

Transition metal anchored on C_9N_4 as a single-atom catalyst for CO_2 hydrogenation:A first-principles study

Jia-Liang Chen(陈嘉亮), Hui-Jia Hu(胡慧佳), and Shi-Hao Wei(韦世豪)
Citation: Chin. Phys. B, 2022, 31 (**10**): 107306. DOI: 10.1088/1674-1056/ac6158
Journal homepage: http://cpb.iphy.ac.cn; http://iopscience.iop.org/cpb

What follows is a list of articles you may be interested in

Prediction of quantum anomalous Hall effect in $CrI_3/ScCl_2$ bilayer heterostructure

Yuan Gao(高源), Huiping Li(李慧平), and Wenguang Zhu(朱文光)
Chin. Phys. B, 2022, 31 (**10**): 107304. DOI: 10.1088/1674-1056/ac67cb

Hexagonal boron phosphide and boron arsenide van der Waals heterostructure as high-efficiency solar cell

Yi Li(李依), Dong Wei(魏东), Gaofu Guo(郭高甫), Gao Zhao(赵高), Yanan Tang(唐亚楠), and Xianqi Dai(戴宪起)
Chin. Phys. B, 2022, 31 (**9**): 097301. DOI: 10.1088/1674-1056/ac6b2a

Half-metallicity induced by out-of-plane electric field on phosphorene nanoribbons

Xiao-Fang Ouyang(欧阳小芳) and Lu Wang(王路)
Chin. Phys. B, 2022, 31 (**7**): 077304. DOI: 10.1088/1674-1056/ac560d

Bias-induced reconstruction of hybrid interface states in magnetic molecular junctions

Ling-Mei Zhang(张令梅), Yuan-Yuan Miao(苗圆圆), Zhi-Peng Cao(曹智鹏), Shuai Qiu(邱帅), Guang-Ping Zhang(张广平), Jun-Feng Ren(任俊峰), Chuan-Kui Wang(王传奎), and Gui-Chao Hu(胡贵超)
Chin. Phys. B, 2022, 31 (**5**): 057303. DOI: 10.1088/1674-1056/ac3caf

Spin—orbit stable dirac nodal line in monolayer B_6O

Wen-Rong Liu(刘文荣), Liang Zhang(张亮), Xiao-Jing Dong(董晓晶), Wei-Xiao Ji(纪维霄), Pei-Ji Wang(王培吉), and Chang-Wen Zhang(张昌文)
Chin. Phys. B, 2022, 31 (**3**): 037305. DOI: 10.1088/1674-1056/ac4cba

---

Transition metal anchored on C_9N_4 as a single-atom catalyst for CO_2 hydrogenation: A first-principles study

Jia-Liang Chen(陈嘉亮)[1], Hui-Jia Hu(胡慧佳)[2], and Shi-Hao Wei(韦世豪)[1,†]

[1] *Department of Microelectronic Science and Engineering, School of Physical Science and Technology, Ningbo University, Ningbo* 315211, *China*
[2] *Department of Electronic and Information Engineering, School of Electrical Engineering and Computer Science, Ningbo University, Ningbo* 315211, *China*

(Received 30 December 2021; revised manuscript received 23 March 2022; accepted manuscript online 28 March 2022)

To alleviate the greenhouse effect and maintain the sustainable development, it is of great significance to find an efficient and low-cost catalyst to reduce carbon dioxide (CO_2) and generate formic acid (FA). In this work, based on the first-principles calculation, the catalytic performance of a single transition metal (TM) (TM = Cr, Mn, Fe, Co, Ni, Cu, Zn, Ru, Rh, Pd, Ag, Cd, Ir, Pt, Au, or Hg) atom anchored on C_9N_4 monolayer (TM@C_9N_4) for the hydrogenation of CO_2 to FA is calculated. The results show that single TM atom doping in C_9N_4 can form a stable TM@C_9N_4 structure, and Cu@C_9N_4 and Co@C_9N_4 show better catalytic performance in the process of CO_2 hydrogenation to FA (the corresponding maximum energy barriers are 0.41 eV and 0.43 eV, respectively). The partial density of states (PDOS), projected crystal orbital Hamilton population (pCOHP), difference charge density analysis and Bader charge analysis demonstrate that the TM atom plays an important role in the reaction. The strong interaction between the 3d orbitals of the TM atom and the non-bonding orbitals ($1\pi_g$) of CO_2 allows the reaction to proceed under mild conditions. In general, our results show that Cu@C_9N_4 and Co@C_9N_4 are a promising single-atom catalyst and can be used as the non-precious metals electrocatalyst for CO_2 hydrogenation to formic acid.

Keywords: first-principles calculation, CO_2 hydrogenation, catalysts, electronic structure, reaction mechanisms, reaction paths

PACS: 73.22.–f, 82.20.Kh **DOI:** 10.1088/1674-1056/ac6158

1. Introduction

How to effectively alleviate the greenhouse effect has always been a source of concern around the world. With the rapid development of industry and society, human activities such as automobile exhaust and fossil fuel consumption are inevitably accompanied by a large amount of carbon dioxide (CO_2) emissions.[1–3] As we all know, the increase of CO_2 emissions is the main factor of the global greenhouse effect.[4–6] At present, capture, chemical absorption and electrocatalysis are mainly used to reduce the amount of CO_2 in the atmosphere.[7] Electrocatalysis has attracted much attention because of its low cost, large-scale application and sustainability. Furthermore, in addition to the hydrogenation of CO_2, the content of CO_2 can also be controlled. Other methods, such as photocatalysis and CO_2 electrolysis, can also produce valuable by-products, e.g., methane, formic acid (FA), methanol, etc.[8–10] FA is widely used in chemistry, industry, medicine and other fields,[11–13] so both experimental research and theoretical calculations are dedicated to finding new catalytic materials to convert CO_2 into FA.[14–19] Unfortunately, due to the high cost, low catalytic efficiency, and harsh external reaction conditions required for different CO_2 hydrogenation catalytic materials, it is difficult to achieve under normal temperature conditions. As a result, finding a suitable catalytic material for CO_2 hydrogenation to formic acid is still a very valuable research.

Since the single-layer graphene is successfully separated,[20,21] carbon-based materials have been widely studied as a substrate with excellent catalytic effects in substances conversion.[22–30] Obviously, because of excellent properties, such as inherent thermal stability, semiconductivity, and cheapness, great efforts have been made to find a carbon-based catalyst that can convert CO_2 into FA.[31–36] However, considering that carbon itself is inert to certain electrochemical reactions, pyrolysis is usually used in experiments to prepare transition metal (TM) and nitrogen-doped carbon-based materials.[43,44] Some carbon atoms in the carbon-based materials are replaced by nitrogen atoms to form carbon nitrogen (CN) materials, which not only retains the original stability, but also provides ideal sites for metal atoms due to the electron pairs of nitrogen atoms. For example, the high throughput single photon excitation pathways, photocatalytic hydrogen and oxygen release, and Au deposition over WO_3/g-C_3N_4 Z-scheme heterojunction have all been investigated.[39–41] Furthermore, the doping-induced method significantly improves the photocatalytic activity and organic matter degradation ability of g-C_3N_4.[42,43] In experiments, common methods, such as chemical vapor deposition, alkaline activation and thermal stripping method, wet chemical method and salt fusion synthesis, are utilized to generate CN

†Corresponding author. E-mail: weishihao@nbu.edu.cn

© 2022 Chinese Physical Society and IOP Publishing Ltd

materials.[44–46] In addition, since $Pt_1@FeO_x$ is firstly proposed to be used in electrocatalysis,[47] single-atom catalysts (SACs) have become the research frontier. Similarly, there are many methods for preparing SACs of CN materials. For example, Co-NG sheet is generated by sonication and heat treatment, and Fe/N/graphene monolayer are prepared by ball milling, demonstrating that CN materials can be employed as substrate for SACs.[48,49] Many studies have shown that SACs formed by doping CN materials with metal atoms have better reactivity and selectivity.[50–58] For instance, Yuan *et al.* reported that, compared with pure CN samples, doping Ni atoms in N-doped carbon nanosheets can significantly improve the CO_2 conversion performance.[59] Ma *et al.* reported that Cu doping in C_2N has good stability and satisfactory performance (the highest barrier is only 0.53 eV) of CO_2 hydrogenation into FA using density functional theory (DFT).[60] Li *et al.* analyzed and summarized the catalytic effects of SACs formed by different 2D single-layer nanosheet doped with Cr, Mn, Fe, Co, Ni, Cu, and Zn on CO_2 hydrogenation from experimental and theoretical perspectives, indicating that SACs have exhibited comparable catalytic performance to the noble-metal benchmarks.[61] So far, although SACs have shown great potential in CO_2 hydrogenation, the research on CO_2 hydrogenation is still in its infancy and needs further exploration.

The above studies fully show that SACs formed by TM-doped CN material are promising candidate for hydrogenation of CO_2 to form FA. Therefore, it is of great significance to find a suitable new CN material as the TM atom carrier. Fortunately, Niu's group just predicted a new type of CN material, C_9N_4.[62] The calculation results show that, compared with other CN materials synthesized in the experiment (such as C_2N, g-C_3N_4), C_9N_4 formation energy is lower,[63–65] which means that it is very possible to experimentally synthesis C_9N_4 and generate SACs utilizing current experimental methods. Therefore, we have carried out the research on the hydrogenation of CO_2 to FA catalyzed by TM doped C_9N_4 and explained its catalytic mechanism, hoping to provide a little bit of help for the experimental synthesis SACs based on C_9N_4.

In order to find a good catalyst for CO_2 hydrogenation to formic acid and clarify its corresponding catalytic mechanism, we study the CO_2 hydrogenation performance of sixteen different TM (TM = Cr, Mn, Fe, Co, Ni, Cu, Zn, Ru, Rh, Pd, Ag, Cd, Ir, Pt, Au, and Hg) atom doped into the C_9N_4 monolayer. Our research results show that $Cu@C_9N_4$ has the best catalytic performance, and its maximum energy barrier is only about 0.41 eV. In addition, We also find three other systems ($Co@C_9N_4$, $Ir@C_9N_4$ and $Ni@C_9N_4$) also have excellent catalytic effects in the hydrogenation of CO_2, and their maximum energy barriers are all less than 0.50 eV, which is lower than that of Ma *et al.*[60] All of the above shows that C_9N_4 is a new type of realizable 2D CN material with promising prospects.

2. Computation details

In our work, all chemical spin-polarized density functional theory (DFT) calculations are performed by using the projector augmented wave (PAW) potentials as implemented in the Vienna *ab initio* simulation package (VASP).[66–68] And the generalized gradient approximation (GGA) with the Perdew–Burke–Ernzerhof (PBE) exchange–correlation energy density functionals is adopted.[69,70] To describe the electron-exchange correction effect, van der Waals (vdW) of DFT-D3 method is adopted.[71] The plane wave basis sets with a kinetic energy cutoff of 500 eV are used. The $3 \times 3 \times 1$ Monkhorst–Pack mesh is used in sampling the Brillouin zone. A vacuum space of 20 Å is adopted to avoid the interactions between adjacent layers. The energy and force of structural geometry optimization are accurate to 10^{-5} eV and 10^{-2} eV, respectively. Isobaric–isothermal (NPT) ensemble molecular dynamics (MD) simulations are carried out at 300 K and 1000 K with an integration step of 1 fs. The diffusion and reaction of the system are invested along the minimum energy path (MEP) with the climbing image nudged elastic band (CI-NEB) method.[72]

The adsorption energy (E_{ads}) is defined as

$$E_{ads} = E_{total} - E_{surface} - E_{adsorbate}, \tag{1}$$

where $E_{adsorbate}$, $E_{surface}$ and E_{total} represent the energy of adsorbate, surface and complex of surface and adsorbate, respectively.

The cohesive energy (E_{coh}) can be obtained by

$$E_{coh} = E_{bulk}/n - E_{single-atom}, \tag{2}$$

where E_{bulk} and $E_{single-atom}$ represent the energy of TM crystal and a single TM atom, respectively. And n is the number of TM atoms in the TM crystal.

3. Result and discussion

3.1. Stability of TM@C_9N_4

After optimized, the lattice constant of the C_9N_4 unit cell is $a = b = 9.64$ Å, which contains 18 carbon atoms and 8 nitrogen atoms. If the radius of N atom is not considered here, the diameter of the hole formed by six nitrogen atoms is about 5.51 Å (see Fig. 1(a)), coinciding with previous reports.[74,74] Because of the large size of the hole, it provides many chemically active sites. The nitrogen atoms in the hole have lone pair electrons, which is the reason why TM atom can be firmly combined with the substrate. As shown in Fig. 1(a), thirteen possible anchoring sites are taken into consideration: S1–S13, and the blue and orange dots indicate that adsorption sites are on the same plane as C_9N_4 and adsorption sites are above C_9N_4, respectively. All metal atoms are investigated on these sites, and finally three different most stable adsorption modes

are found, as shown in Fig. 2. It is found that Cr, Mn, Fe, Co, Ni, Cu, Zn, Ru, Rh, Pd, Cd, Ir, and Pt tend to bond with two nitrogen atoms and lie in the same plane with the substrate (Fig. 2(a)). At the same time, Ag, Au and Hg are located in the center of the hole (Figs. 2(b) and 2(c)). The difference is that Au or Ag is coplanar with C_9N_4 monolayer, while Hg is above the C_9N_4 monolayer (the vertical distance between Hg and C_9N_4 monolayer is about 1.06 Å). The adsorption energy between TM atom and C_9N_4 monolayer is shown in Fig. S1 and Table S1. The large adsorption energy (all great that 2.0 eV) indicates the formation of a strong chemical bond (except for Hg). The stability of SACs is further confirmed by MD simulations. We calculate the stability of six TM@C_9N_4 (TM = Co, Ni, Cu, Ru, Rh, and Ir) and find that they all have satisfactory stability. For example, as shown in Figs. S2 and S3, the structures of Cu@C_9N_4 has no obvious change at 300 K and 1000 K, and the energy fluctuation is minor. In addition, we also calculate the partial density of states (PDOS) of TM@C_9N_4 (Fig. S4). It is found that there is a strong orbitals hybridization between the d orbitals of TM atom and the p orbitals of the nitrogen atoms near the Fermi level. These results further confirm that TM atom can be firmly anchored to the hole of C_9N_4. This conclusion is also confirmed by the charge transfer between TM atom and C_9N_4 and the diffusion barrier of TM atom on C_9N_4. For simplicity, here, Cu atom is adsorbed on C_9N_4 as an example. Obviously, as shown in Fig. 1(b), the charge is transferred from Cu atom to N atoms. The Bader charge analysis shows that about 0.75 electrons are transferred from Cu atom to C_9N_4, where the single N atom connected to Cu atom gets about 0.31 electrons. We also find that, as shown in Fig. S5, if the adsorbed Cu atom leaves the adsorption position, it needs to overcome the energy of 3.24 eV or 3.16 eV, which indicates that the adsorbed Cu atom is difficult to move from the hole to the adjacent hexagonal adsorption position composed of C and N atoms. In addition, as shown in Table S1, a ratio of adsorption energy to cohesive energy is greater than 0.5, which means that TM atoms are not easy to form clusters during the reaction and influencing the activity of the catalyst.[75,76] Therefore, TM@C_9N_4 can be regarded as a stable CO_2 hydrogenation catalyst.

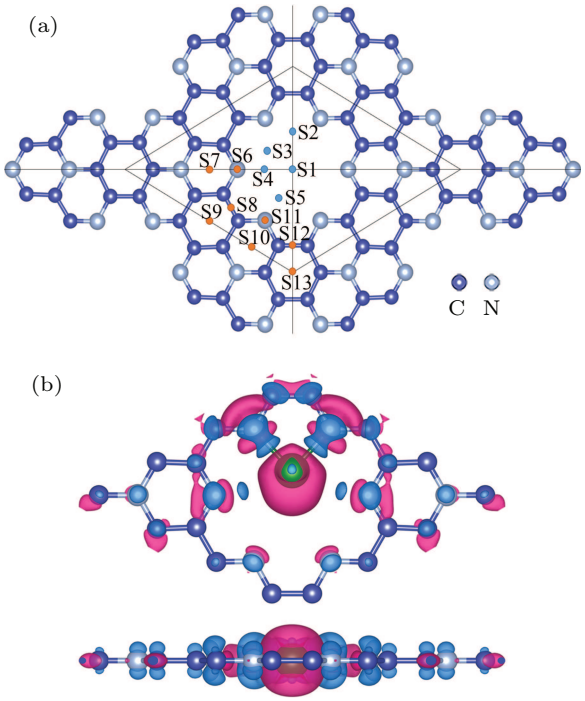


Fig. 1. (a) S1–S13 represent the adsorption position of adsorbed metal atom on C_9N_4, where the solid parallelogram represents the C_9N_4 unit cell, and (b) the difference charge density of Cu atom adsorbed on C_9N_4, where the isosurface value is set to be 0.003 $e/Å^3$, and the blue and red isosurfaces represent the accumulation and consumption of electrons, respectively.

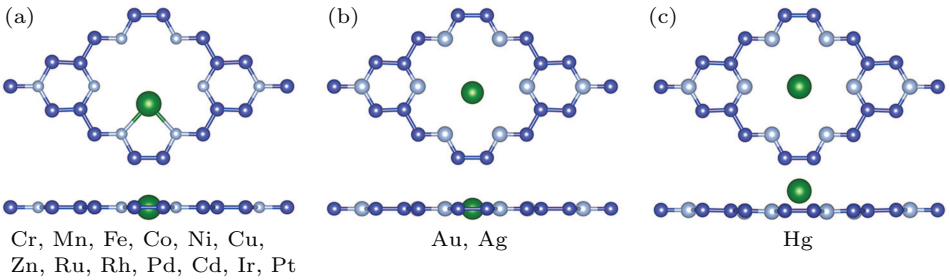


Fig. 2. (a)–(c) The most stable state of the adsorption state of sixteen metals.

3.2. Adsorption of H_2 and CO_2 molecules on TM@C_9N_4

It is well known that gas adsorption has a great influence on its subsequent electrocatalytic process. Therefore, the side-on and end-on adsorption patterns of H_2 and CO_2 gas molecules on the catalyst are investigated. The optimal adsorption energies for H_2 ($E_{ads}^{H_2}$), CO_2 ($E_{ads}^{CO_2}$) and H_2+CO_2 ($E_{ads}^{H_2+CO_2}$) adsorbed on TM@C_9N_4 are shown in Table 1. For Cr, Mn, Fe, Zn, Pd, Ag, Cd, Pt, Au and Hg, $E_{ads}^{CO_2}$ is much greater than $E_{ads}^{H_2}$, which means that CO_2 will be firmly adsorbed on the catalyst surface and lead to catalyst poisoning by CO_2. At the same time, for Co, Ni, Cu, Ru, Rh, and Ir, $E_{ads}^{CO_2}$ is much smaller than $E_{ads}^{H_2}$, which means that the six TM atoms are suitable candidates for doping C_9N_4 to form catalysts. Therefore, we will only discuss the six catalysts (Co@C_9N_4, Ni@C_9N_4, Cu@C_9N_4, Ru@C_9N_4, Rh@C_9N_4, and Ir@C_9N_4).

Table 1. The adsorption energy (eV) of H_2 ($E_{ads}^{H_2}$), CO_2 ($E_{ads}^{CO_2}$) and $H_2 + CO_2$ ($E_{ads}^{H_2+CO_2}$) for the most favorable gas adsorption. The bond length (Å) of H–H for H_2 molecule singly adsorbed ($D_{H-H}^{H_2}$) and H_2+CO_2 co-adsorbed ($D_{H-H}^{H_2+CO_2}$) on TM@C_9N_4. $D_{CO_2-Surface}^{H_2+CO_2}$ is the vertical height of CO_2 from TM@C_9N_4 at the co-adsorption state. The red font represents that $E_{ads}^{H_2}$ is greater than $E_{ads}^{CO_2}$.

	Cr	Mn	Fe	Co	Ni	Cu	Zn	Ru	Rh	Pd	Ag	Cd	Ir	Pt	Au	Hg
$E_{ads}^{H_2}$	–0.17	–0.24	–0.33	–0.48	–0.45	–0.60	–0.17	–0.67	–0.46	–0.30	–0.09	–0.14	–0.75	–0.35	–0.09	–0.06
$E_{ads}^{CO_2}$	–0.39	–0.49	–0.52	–0.40	–0.34	–0.36	–0.56	–0.33	–0.23	–0.55	–0.23	–0.50	–0.22	–0.50	–0.22	–0.31
$E_{ads}^{H_2+CO_2}$	–0.35	–0.48	–0.55	–0.65	–0.60	–0.79	–0.39	–0.82	–0.55	–0.57	–0.12	–0.30	–0.88	–0.61	–0.12	0.84
$D_{H-H}^{H_2}$	0.77	0.77	0.79	0.81	0.82	0.83	0.77	0.83	0.85	0.80	0.76	0.77	0.93	0.80	0.76	0.75
$D_{H-H}^{H_2+CO_2}$	0.77	0.77	0.78	0.80	0.83	0.83	0.77	0.83	0.83	0.81	0.76	0.77	0.92	0.81	0.76	0.75
$D_{CO_2-Surface}^{H_2}$	2.06	2.08	2.09	2.14	2.10	2.19	2.05	2.01	2.04	2.11	2.15	2.10	2.07	2.09	2.22	2.26
$D_{CO_2-Surface}^{H_2+CO_2}$	3.12	3.16	3.14	3.28	3.14	3.28	3.12	3.02	3.10	3.16	3.27	3.20	3.10	3.16	3.30	3.36

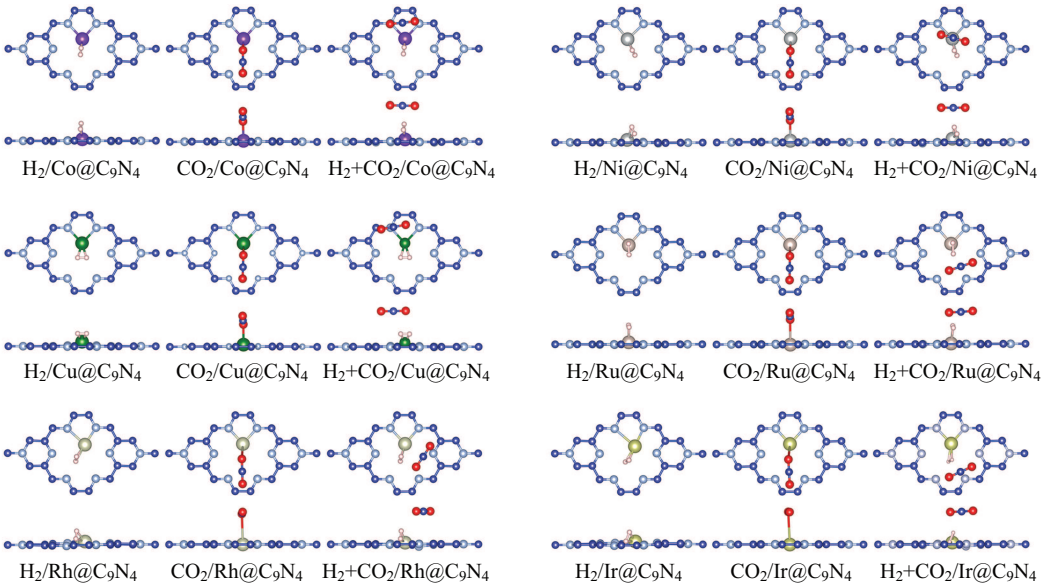


Fig. 3. The optimized geometric structures for TM@C_9N_4 (TM = Co, Ni, Cu, Ru, Rh, Ir) adsorbing (a) H_2, (b) CO_2, and (c) H_2+CO_2.

The optimized geometric structures for TM@C_9N_4 (TM = Co, Ni, Cu, Ru, Rh, and Ir) adsorbing H_2, CO_2 and H_2+CO_2 are shown in Fig. 3. While H_2 molecule is singly adsorbed on TM@C_9N_4, the H–H bond length has different degree of elongation, ranging from 0.81 Å to 0.93 Å (the H–H bond length of free H_2 is 0.75 Å), which indicates that H_2 molecule is activated in varying degrees and conducive to the fractures of H–H bond. When H_2 and CO_2 are simultaneously adsorbed to TM@C_9N_4, as shown in Fig. 3, H_2 is still directly adsorbed on TM atom, and the adsorption pattern and H–H bond are almost the same as the H_2 molecule singly adsorbed on TM@C_9N_4. At this time, the adsorption energy increases slightly (as shown in Table 1). What is more, the CO_2 molecule floats above the surface of the catalyst, the distances between CO_2 and the surface of catalyst ($D_{CO_2-Surface}^{H_2+CO_2}$), as shown in Table 1, are all greater than 3.0 Å. At the same time, from the differential charge density of H_2 and CO_2 co-adsorbed on Cu@C_9N_4 (shown in Fig. S6), it can be seen that there is almost no charge transfer between CO_2 and the catalyst. It is due to the fact that $E_{ads}^{H_2}$ is greater than $E_{ads}^{CO_2}$ (shown in Table 1), and there is no active adsorption site to adsorb CO_2 when H_2 molecule is firstly adsorbed on Cu@C_9N_4. Therefore, we can conclude that CO_2 interacts with the catalyst in the form of physical adsorption at co-adsorption state.

3.3. CO_2 hydrogenation on TM@C_9N_4

According to different adsorption conditions, the adsorption of H_2 alone (named Path I) and the co-adsorption of H_2 and CO_2 (named Path II) on TM@C_9N_4 (TM = Co, Ni, Cu, Ru, Rh and Ir) are studied as follows:

Path I: $H_2 + * \rightarrow *H\text{–}H* \rightarrow *H + H* \rightarrow *H + H* + CO_2 \rightarrow OCHO* + H* \rightarrow HCOOH* \rightarrow HCOOH + *$;

Path II: $H_2 + CO_2 + * \rightarrow *H\text{–}H* + CO_2 \rightarrow *H + H* + CO_2 \rightarrow HOCO* + H* \rightarrow HCOOH^* \rightarrow HCOOH + *$,

where $*$ denotes the catalyst.

The structure of the initial state (IS), intermediate state (MS), transition state (TS) and final state (FS) and the energy change along the MEP are shown in Figs. 4 (for Path I), S7 (for Path II) and Table S2. The energy fluctuation diagram of CO_2 hydrogenation on Cu@C_9N_4 and the number of images of CI-NEB calculated at each step are shown in Fig. S8. As shown in Fig. S7 and Table S2, considering that the energy barriers of the rate-limiting step (RLS) in Path II are greater than 1.60 eV, this means that the reaction along the Path II is

difficult to occur at room temperature. For the sake of simplicity, we take Cu@C_9N_4 in Path I as an example in the following discussion. First of all, in the IS, a H_2 molecule is adsorbed on Cu@C_9N_4. According to the previous analysis, the H–H bond is activated to a certain extent after the adsorption, so the fracture of H–H bond in the first TS (TS1) only needs to overcome 0.21 eV energy barrier and reach the first MS (MS1). In the MS1, one of the H atoms in H_2 molecule still forms a bond with the Cu atom (the bond length of H–Cu is about 1.51 Å), the other H atom approaches to the N atom in the six nitrogen hole, forming a N–H bond (1.04 Å), at the same time, the bond length of H–H is extended from 0.83 Å to 0.99 Å. For the MS1+CO_2 state, a CO_2 molecule is adsorbed from outside. Next, in the second TS (TS2), the Cu–H bond length extends from 1.51 Å to 1.61 Å, and the energy barrier of 0.41 eV needs to be overcome when CO_2 molecule approaches the catalyst. After reaching the highest point of energy, CO_2 spontaneously forms bond with Cu atom and releases energy, forming Cu–O bond (1.87 Å). Cu–H bond is broken to form H–C bond (1.12 Å). Then in the third TS (TS3), the N–H bond (1.06 Å) is broken and the H atom approaches to the O atom, forming a H–O bond (1.07 Å), and then forming a FA on the surface of the catalyst. In the whole electrocatalysis process, the highest energy barrier is 0.41 eV. So, the hydrogenation of CO_2 to FA through the Path I is relatively easy to achieve at room temperature, which is consistent with the results of Kathalikkattil *et al.*[77] In addition, we also notice that the highest energy barrier of Co@C_9N_4, Ir@C_9N_4 and Ni@C_9N_4 are 0.43 eV, 0.46 eV and 0.48 eV, respectively, which are less than 0.5 eV. While the highest energy barrier of Rh@C_9N_4 is only about 0.51 eV. Just like Cu@C9N4, their RLS is in MS1+CO_2→TS2.

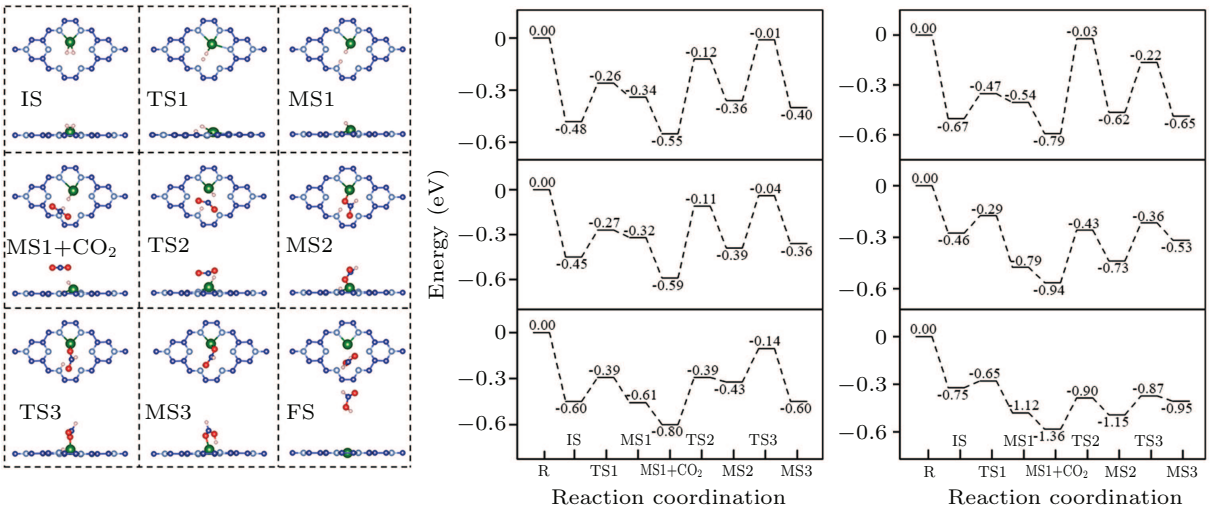


Fig. 4. The structure of the intermediate and transition state of Cu@C_9N_4 (left) and the potential energy profile of TM@C_9N_4 (TM = Co, Ni, Cu, Ru, Rh, Ir) (right) in Path I.

In addition, we also consider other possible reduction reactions, such as the hydrogenation of CO_2 to methane or methanol. But in fact, whether it is to generate methane or methanol, it must first reduce CO_2 to CO, namely, $CO_2 + H_2 \rightarrow CO + H_2O$. Taking MS1+$CO_2$ in Path I as the initial state (IS), the corresponding structure and energy change along the MEP for CO_2 reduction are shown in Fig. S9. It can be seen that there are two large energy barriers in the whole process, which are 1.38 eV and 0.71 eV, respectively. Therefore, the reduction of CO_2 to methanol or methane is less competitive than the hydrogenation of CO_2 to formic acid.

4. Property analysis

As mentioned above, considering that Cu@C_9N_4 and Co@C_9N_4 have excellent catalytic performance, the partial density of states (PDOS), projected crystal orbital Hamilton population (pCOHP) and charge transfer between adsorbed gas molecule (H_2 or CO_2) and catalysts for TM@C_9N_4 (TM = Co, Ni, Cu, Ru, Rh, and Ir) are performed to further clarify the catalytic mechanism. Figure 5 shows the PDOS and pCOHP of the transition state TS2 of Co@C_9N_4 (a) and Cu@C_9N_4 (b) in Path I, and Co@C_9N_4 (c) and Cu@C_9N_4 (d) in Path II, respectively. It is obvious find that, from Figs. 5(a) and 5(b), the 3d orbitals of Cu or Co atom are strongly hybridized with the molecular orbitals of CO_2 near the Fermi level in Path I. At the same time, in Path II, near the Fermi level, the hybridization between 3d orbitals of Cu or Co atom and CO_2 molecular orbitals are much weaker, which can be clearly seen from Figs. 5(c) and 5(d). We can further confirm this conclusion from pCOHP. As shown in Fig. 5, the hybridized energy levels of TM-3d orbitals and CO_2 orbitals split into the bonding and anti-bonding states. The anti-bonding states for Co@C_9N_4 (a) and Cu@C_9N_4 (b) in Path I are all above the Fermi level, while the anti-bonding states of Co@C_9N_4 (c) and Cu@C_9N_4 (d) in Path II are partly under Fermi level. In other words, the interaction between CO_2 and TM@C_9N_4 gets weakened by the

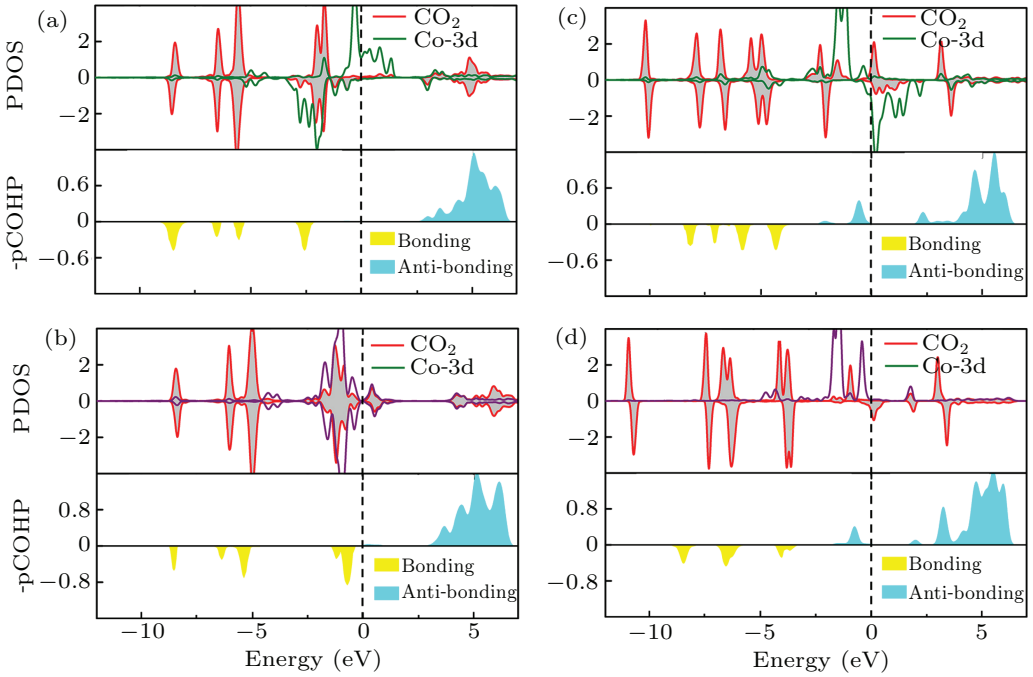


Fig. 5. The partial density of states (PDOS) and projected crystal orbital Hamilton population (pCOHP) for the transition state TS2 of Co@C_9N_4 (a) and Cu@C_9N_4 (b) in Path I, and Co@C_9N_4 (c) and Cu@C_9N_4 (d) in Path II, respectively. The Fermi level is set to 0 eV.

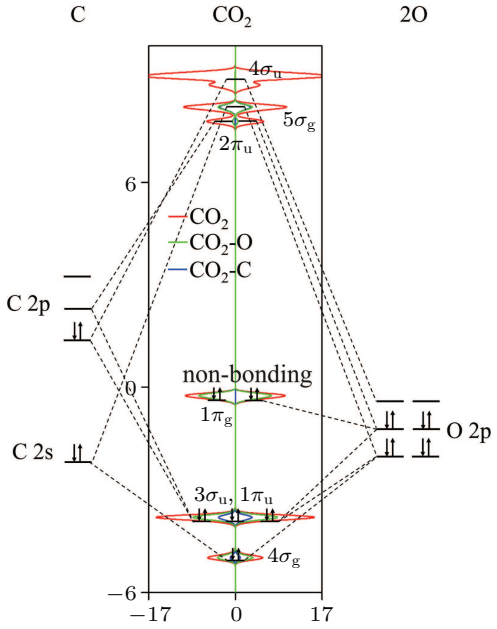


Fig. 6. The calculated PDOS of CO_2 and the schematic molecule orbitals energy level diagram of the interaction between C and O atoms. The Fermi level is set to 0 eV.

anti-bonding population entering below the Fermi level. This means that the activation of CO_2 in Path I is stronger than that in Path II. So the energy barriers in Path I are much smaller than those in Path II.

It is worth noting that the RLS in the catalytic reactions of all systems is MS1+CO_2 → TS2 (shown in Fig. 4), which is due to the fact that CO_2 molecule has a special $1\pi_g$ orbitals, that is, non-bonding orbitals. As shown in Fig. 6, the molecular orbitals of free CO_2 molecule, mainly including $4\sigma_g$, $3\sigma_u$, $1\pi_u$, $1\pi_g$, $2\pi_u$, $5\sigma_g$ and $4\sigma_u$. $1\pi_g$ and $2\pi_u$ orbitals, which corresponds to the highest occupied orbitals (HOMO) and the lowest unoccupied orbitals (LUMO), respectively, are the main participants in the catalytic activation of CO_2. However, as shown in Fig. 6, the delocalized $1\pi_g$ bond does not hybridize with C atom, which is only composed of 2p orbitals of two oxygen atoms, so it is a non-bonding orbitals. Moreover, CO_2 molecule does not have a lone pair of electrons. So the electrons on HOMO have poor activity, resulting in poor chemical activity of CO_2, when CO_2 reacts with the catalyst. Therefore, the RLS (MS1+CO_2 → TS2) is the process in which CO_2 participates in the reaction, and the strength of the interaction between the $1\pi_g$ orbitals and the catalyst determines the difficulty of this reaction.

The PDOS of TS2 for the TM@C_9N_4 (TM = Co, Ni, Cu, Ru, Rh, and Ir) in Path I are shown in Fig. 7. As shown in Fig. 7(c), near the Fermi energy level, there is significant hybridization between the 3d orbitals of Cu atom and the $1\pi_g$ orbitals of CO_2. So, in the process from MS1+CO_2 to TS2, the C=O bond of CO_2 is extended from 1.17 Å to 1.23 Å, which means CO_2 molecule is activated on the Cu@C_9N_4. While the H–Cu bond is broken from TS2 to MS2 (as shown in Fig. 4), resulting that CO_2 maybe replace the position of H to form a bond with Cu. For Co@C_9N_4, we also find the same hybridization mechanism from Fig. 7(a). We also notice that, for Ni@C_9N_4, the hybrid interaction between the 3d orbitals of Ni atom and the $1\pi_g$ orbitals of CO_2 is much weaker than that of Cu or Co atom, which leads to a larger energy barrier (0.48 eV).

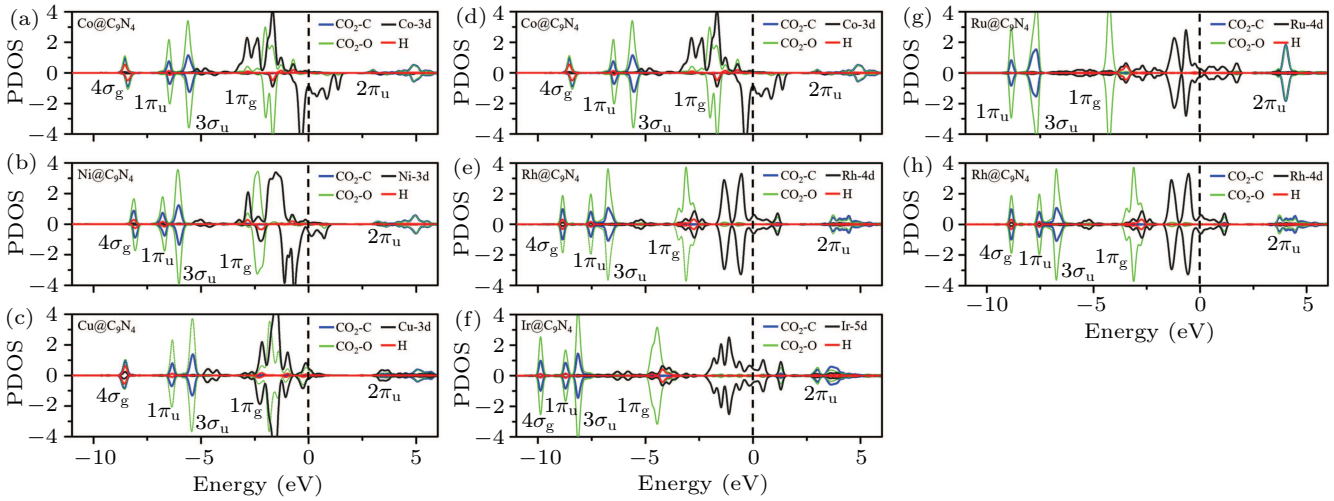


Fig. 7. The partial density of states (PDOS) for the TM-*n*d ($n = 3, 4, 5$), C, O and H of the transition state (TS2) in Path I. The black, blue, green and red lines represent the TM-*n*d, carbon, oxygen and hydrogen atoms, respectively. The vertical dash-dotted lines correspond to the Fermi level (set to 0 eV). For the convenience of comparison, the PDOS of Co@C_9N_4 is plotted twice.

We notice that Co, Rh and Ir are also the same group of TM atoms in the periodic table of elements, and the hybridization of the 3d orbitals of Co atom with the $1\pi_g$ orbitals of CO_2 molecule are more obvious than Rh and Ir, while the hybridization of H and Co is relatively weak. The result indicates that the rupture of the Co–H bond and CO_2 activation are less obstructive for Co@C_9N_4. So the RLS barrier of Co@C_9N_4 (0.43 eV) is lower than that of Rh@C_9N_4 (0.46 eV) and Ir@C_9N_4 (0.51 eV). The hybridization between CO_2 and Rh, Ir atoms is also similar. As shown in Figs. 7(e) and 7(f), the hybrid interaction between 5d orbitals of Ir atom and $1\pi_g$ orbitals of CO_2 is slightly stronger than that of Rh atom, which leads to that the energy barrier of Ir@C_9N_4 (0.46 eV) is lower than that of Rh@C_9N_4 (0.51 eV). Finally, in the PDOS of Ru and Rh (see Figs. 7(g) and 7(h)) in the same period, the $1\pi_g$ orbitals of CO_2 on Ru@C_9N_4 remain narrow and isolated. The weaker interaction between CO_2 and Ru in the RLS of Ru@C_9N_4 confirms that Ru@C_9N_4 has the worst catalytic performance and the highest energy barrier in these six systems.

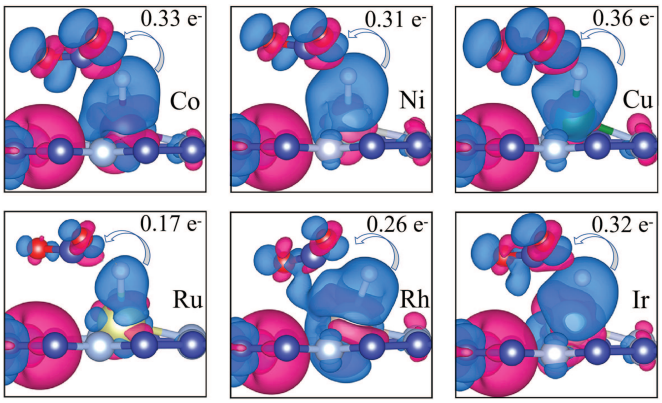


Fig. 8. Difference charge density of CO_2 molecule adsorbed on six TM@C_9N_4 (TM = Co, Ni, Cu, Ru, Rh and Ir) for the transition state TS2 in Path I, respectively. Red and blue represent charge accumulation and depletion, respectively. The isosurfaces is set to be 0.004 $e/Å^3$.

Additionally, the Bader charge analysis and difference charge density are also performed to calculate the charge transfer between the catalyst and CO_2. The charge transfer is observed in Fig. 8 from TM atom to CO_2. And the relationship between the energy barrier and the number of electrons obtained by CO_2 from the catalyst is shown in Fig. 9. It can be seen that the number of electrons transferred is inversely proportional to the value of the energy barrier that needs to be overcome in the RLS. In other words, the more significant the interaction between CO_2 and TM@C_9N_4, the easier it is for the electrons on the d orbitals of the TM atom to be transferred to the CO_2 molecule to activate CO_2.

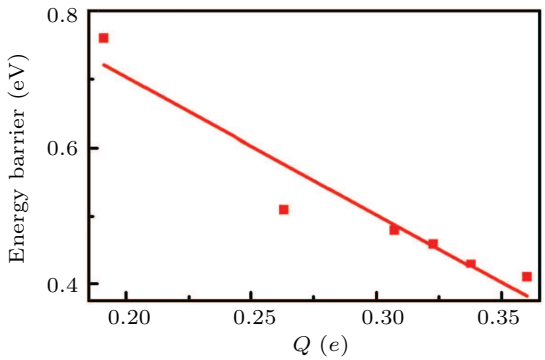


Fig. 9. The change of energy barriers as function of the number of electrons (Q) transferred from catalyst to CO_2 for the TS2 in Path I.

Furthermore, we also considered the possibility of the aggregation of two TM atoms in the cavity of C_9N_4. The optimized structures of the co-adsorption of two TM atoms are shown in Fig. S10. It is interesting to find that two TM atoms are located on two sides of C_9N_4, respectively. It means that, in the process of CO_2 hydrogenation, a single TM atom still plays a key role. At the same, the energy barrier of RLS for the co-adsorption of two TM atoms is much larger than that of the single TM atom in the CO_2 hydrogenation catalytic reactions.

5. Conclusion

In general, based on the first-principles calculation, we have studied the catalytic effect of a series of TM (TM = Cr, Mn, Fe, Co, Ni, Cu, Zn, Ru, Rh, Pd, Ag, Cd, Ir, Pt, Au, and Hg) doped with C_9N_4 on CO_2 hydrogenation. Because of the abundant chemically active sites with lone pairs provided by the 6N hole, TM can be stably doped on C_9N_4. The extremely high diffusion barrier of Cu atom (3.21 eV or 3.16 eV), results of MD simulations and the strong interaction between TM atom and C_9N_4 demonstrate the catalytic performance and stability of the catalyst. It is interesting to find that, except for the six TM atoms (Co, Ni, Cu, Ru, Rh and IR), other TM atoms can be poisoned by CO_2. We have discussed the two routes (Path I and Path II) of CO_2 hydrogenation respectively. Our results show that Path I is more in line with our requirements in energy. It is show that among the sixteen TM@C_9N_4 monolayer catalysts, Cu@C_9N_4 and Co@C_9N_4 show better catalytic effects (energy barrier is less than 0.45 eV), which has more advantages over other similar catalysts. The partial density of states (PDOS), projected crystal orbital Hamilton population (pCOHP) and Bader charge analysis for CO_2 and H_2 adsorbed on TM@C_9N_4 further demonstrate the catalytic mechanism: (i) When the H_2 molecule is captured by the catalyst, the hybridization of the s orbitals of H_2 and the 3d orbitals of the TM atom activates the H–H bond and H_2 molecule is significantly elongated. (ii) The stronger the hybridization between the non-bonding orbitals of CO_2 ($1\pi_g$) and the 3d orbitals of TM atom near the Fermi level, the smaller the energy barrier of the rate-limiting step. That is why the Cu@C_9N_4 system has a minimum energy barrier of 0.41 eV in Path I. In short, our research has discovered a achievable non-noble metal 2D single-layer nanosheet catalytic material, which can alleviate the greenhouse effect and form valuable FA product, providing new possibilities for future sustainable development.

Acknowledgements

Project supported by the National Natural Science Foundation of China (Grant No. 51871126) and the K. C. Wong Magna Fund in Ningbo University. The computation was performed in the Supercomputer Center of NBU.

References

[1] Fraccascia L and Giannoccaro I 2019 *J. Clean. Prod.* **234** 1399
[2] Cariou P, Parola F and Notteboom T 2019 *Int. J. Prod. Econ.* **208** 17
[3] Andrew R M 2018 *Earth Syst. Sci. Data* **10** 195
[4] Chen H, Winderlich J, Gerbig C, Hoefer A, Rella C, Crosson E, Van Pelt A, Steinbach J, Kolle O and Beck V 2010 *Atmos. Meas. Tech.* **3** 375
[5] Gerber P, Vellinga T, Opio C and Steinfeld H 2011 *Livest. Sci.* **139** 100
[6] Joos F, Roth R, Fuglestvedt J, Peters G P, Enting I G, Bloh W v, Brovkin V, Burke E J, Eby M and Edwards N R 2013 *Atmos. Chem. Phys.* **13** 2793
[7] Feng Z, Shan D and Gang C 2011 *Chin. Phys. B* **20** 77103
[8] Weekes D M, Salvatore D A, Reyes A, Huang A and Berlinguette C P 2018 *Acc. Chem. Res.* **51** 910
[9] Wang W H, Himeda Y, Muckerman J T, Manbeck G F and Fujita E 2015 *Chem. Rev.* **115** 12936
[10] Hu S L, Zhao Z X and Shi T Y 2013 *Chin. Phys. Lett.* **30** 103103
[11] Valentini F, Kozell V, Petrucci C, Marrocchi A, Gu Y, Gelman D and Vaccaro L 2019 *Energ. Environ. Sci.* **12** 2646
[12] Zhang J and Yan N 2016 *Green Chem.* **18** 5050
[13] Bhat R M, Vidya K and Kamath G 2001 *Int. J. Dermatol* **40** 415
[14] Yu X, and Pickup P G 2008 *J. Power Sources* **182** 124
[15] Schaub T and Paciello R A 2011 *Angew. Chem. Int. Edit.* **50** 7278
[16] Tamaki Y, Morimoto T, Koike K and Ishitani O 2012 *Proc. Natl. Acad. Sci. USA* **109** 15673
[17] McCollom T M and Seewald J S 2003 *Geochim. Cosmochim. Ac.* **67** 3625
[18] He C S, Gong L, Zhang J, He P P and Mu Y 2017 *J. CO_2 Util.* **19** 157
[19] Preti D, Resta C, Squarcialupi S and Fachinetti G 2011 *Angew. Chem.* **123** 12759
[20] Zhang C, He Q, Chu W and Zhao Y 2020 *Appl. Surf. Sci.* **534** 147575
[21] Duplock E J, Scheffler M and Lindan P J D 2004 *Phys. Rev. Lett.* **92** 225502
[22] Mauter M S and Elimelech M 2008 *Environ. Sci. Technol.* **42** 5843
[23] Liu X and Dai L 2016 *Nat. Rev. Mater.* **1** 1
[24] Kong X K, Chen C L and Chen Q W 2014 *Chem. Soc. Rev.* **43** 2841
[25] Kortlever R, Peters I, Koper S and Koper M TM 2015 *Acs. Catal.* **5** 3916
[26] Liu X, Jiao Y, Zheng Y, Jaroniec M and Qiao S Z 2019 *J. Am. Chem. Soc.* **141** 9664
[27] Peng C S, Zhou Y D, Zhang S S and Zhao Z Y 2021 *Chin. Phys. B* **30** 17101
[28] Zhang D, Lin L Z and Zhu J J 2014 *Chin. Phys. Lett.* **31** 028102
[29] Lin Q M, Zhang X, Lu Q C, Luo Y B, Cui J G, Yan X, Ren X M and Huang X 2019 *Acta Phys. Sin.* **68** 247302 (in Chinese)
[30] Zuo M, Liao W H, Wu D and Lin L E 2019 *Acta Phys. Sin.* **68** 237302 (in Chinese)
[31] Wang Y X, Yang Q, Liu C, Wang G X, Wu M, Liu H, Sui Y M and Yang X Y 2020 *Chin. Phys. B* **37** 58201
[32] Banhart F, Kotakoski J and Krasheninnikov A V 2011 *ACS Nano* **5** 26
[33] Jia Yi, Zhang L, Du A, Gao G, Chen J, Yan X, Brown C L and Yao X 2016 *Adv. Mater.* **28** 9532
[34] Huang H and Wang X 2012 *J. Mater. Chem.* **22** 22533
[35] Wang Z, Yu Z and Zhao J 2018 *Phys. Chem. Chem. Phys.* **20** 12835
[36] Zhu H R, Chen J L and Wei S H 2021 *Chin. Phys. B* **30** 083101
[37] Zhang L, Xiao J, Wang H and Shao M 2017 *Acs Catal.* **7** 7855
[38] Guan B Y, Yu L and Lou X W 2017 *Adv. Sci.* **4** 1700247
[39] Li B, Peng W, Zhang J, Lian J C, Huang T, Cheng N, Luo Z, Huang W Q, Hu W and Pan A 2021 *Adv. Funct. Mater.* **31** 2100816
[40] Zhou B X, Ding S S, Yang K X, Zhang J, Huang G F, Pan A, Hu W, Li K and Huang W Q 2021 *Adv. Funct. Mater.* **31** 2009230
[41] Humayun M, Ullah H, Cao J, Pi W, Yuan Y, Ali S, Tahir A A, Yue P, Khan A, Zheng Z, Fu Q and Luo W 2020 *Nano-Micro Lett.* **12** 1
[42] Li Y Y, Zhou B X, Zhang H W, Ma S F, Huang W Q, Peng W, Hu W and Huang G F 2019 *Nanoscale* **11** 6876
[43] Liu X, Ma R, Zhuang L, Hu B, Chen J, Liu X and Wang X 2021 *Crit. Rev. Env. Sci. Technol.* **51** 751
[44] Wang Y, Liu L, Ma T, Zhang Y and Huang H 2021 *Adv. Funct. Mater.* **31** 2102540
[45] Hu P, Chen C, Zeng R, Xiang J, Huang Y, Hou D, Li Q and Huang Y 2018 *Nano Energy* **50** 376
[46] Tian Z, López-Salas N, Liu, C, Liu T and Antonietti M 2020 *Advanced Science* **7** 2001767
[47] Qiao B, Wang A, Yang X, Allard L F, Jiang Z, Cui Y, Liu J, Li J, Zhang T 2011 *Nat. Chem.* **3** 634
[48] Fei H, Dong J, Arellano-Jiménez M J, Ye G, Dong Kim N, Samuel E L, Peng Z, Zhu Z, Qin F, Bao J, Yacaman M J, Ajayan P M and Chen D 2015 *Nat. Commun.* **6** 1
[49] Liu Q, Liu Y, Li H, Li L, Deng D, Yang F and Bao X 2017 *Appl. Surf. Sci.* **410** 111
[50] Hossain M D, Liu Z, Zhuang M, Yan X and Xu G L 2019 *Adv. Energy Mater.* **9** 1803689
[51] Li J, Zhong L, Tong L, Yu Y, Liu Q, Zhang S, Yin C, Qiao L, Li S and Si R 2019 *Adv. Funct. Mater.* **29** 1905423

[52] Vilé G, Albani D, Nachtegaal M, Chen Z, Dontsova D, Antonietti M, López, N and Pérez-Ramírez J 2015 *Angew. Chem. Int. Edit.* **54** 11265
[53] Jones J, Xiong H, DeLaRiva A T, Peterson E J, Pham H, Challa S R, Qi G, Oh S, Wiebenga M H, Hernández X I P, Wang Y and Datye A K 2016 *Science* **353** 150
[54] Lin J, Wang A, Qiao B, Liu X, Yang X, Wang X, Liang J, Li J, Liu J and Zhang T 2013 *J. Am. Chem. Soc.* **135** 15314
[55] Sirijaraensre J and Limtrakul J 2016 *Appl. Surf. Sci.* **364** 241
[56] Back S, Lim J, Kim N Y, Kim Y H and Jung Y 2017 *Chem. Sci.* **8** 1090
[57] Zhang H, Li Jing, Xi S, Du Y, Hai X, Wang J, Xu H, Wu G, Zhang J and Lu J 2019 *Angew. Chem.* **131** 15013
[58] Cui X, An W, Liu X, Wang H, Men Y and Wang J 2018 *Nanoscale* **10** 15262
[59] Yuan C Z, Liang K, Xia X M, Yang Z K, Jiang Y F, Zhao T, Lin C, Cheang T Y, Zhong S L and Xu A W 2019 *Catal. Sci. Technol.* **9** 3669
[60] Ma J, Gong H, Zhang T, Yu H, Zhang R, Liu Z, Yang G, Sun H, Tang S and Qiu Y 2018 *Appl. Surf. Sci.* **488** 1
[61] Li M, Wang H, Luo W, Sherrell P C, Chen J and Yang J 2020 *Adv. Mater.* **32** 2001848
[62] Mortazavi B, Shahrokhi M and Shapeev A V 2019 *J. Mater. Chem. C* **7** 10908
[63] Groenewolt M and Antonietti M 2005 *Adv. Mater.* **17** 1789
[64] Ma DW, Wang Q, Yan X, Zhang X, He C, Zhou D, Tang Y, Lu Z and Yang Z 2016 *Carbon* **105** 463
[65] Wang D, Han D X, Liu L and Niu L 2016 *Rsc Adv.* **6** 28484
[66] Kresse G and Furthmüller J 1996 *Phys. Rev. B* **54** 11169
[67] Kresse G and Joubert D 1999 *Phys. Rev. B* **59** 1758
[68] Blöchl P E 1994 *Phys. Rev. B* **50** 17953
[69] Perdew J P, Chevary J A, Vosko S H and Jackson K A, Pederson M R, Singh D J and Fiolhais C 1992 *Phys. Rev. B* **46** 6671
[70] Perdew J P and Wang Y 1992 *Phys. Rev. B* **45** 13244
[71] Grimme S, Antony J, Ehrlich S and Krieg H 2010 *J. Chem. Phys.* **132** 154104
[72] Henkelman G, Uberuaga B P and Jónsson H 2000 *J. Chem. Phys.* **113** 9901
[73] He B, Shen J, Lu Z and Ma D 2020 *Appl. Surf. Sci.* **527** 146828
[74] Zhang J, Zhao Y, Wang Z, Yang G, Tian J, Ma D and Wang Y 2020 *New J. Chem.* **44** 422
[75] Chan K T, Neaton J B and Cohen M L 2008 *Phys. Rev. B* **77** 235430
[76] Choi C, Back S, Kim N Y, Lim J, Kim Y H and Jung Y 2018 *Acs Catalysis.* **8** 7517
[77] Kathalikkattil A C, Roshan R, Tharu J, Soek H G, Ryu H S and Par D W 2014 *ChemCatChem* **6** 284